Implementation of a high-order spatial discretization into a finite volume solver: Applications to turbomachinery test cases using an eddy-viscosity turbulence closure

Heliyon 10 (2024) e36478

Contents lists available at ScienceDirect

Heliyon

journal homepage: www.cell.com/heliyon

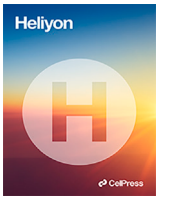

Research article

Implementation of a high-order spatial discretization into a finite volume solver: Applications to turbomachinery test cases using an eddy-viscosity turbulence closure

Nicola Rosafio, Simone Salvadori *, Daniela Anna Misul

Dipartimento Energia, Politecnico di Torino, Corso Duca degli Abruzzi 24, Torino, 10129, TO, Italy

ARTICLE INFO

Keywords:
Turbomachinery
Finite volume method
High-order reconstruction
Computational fluid dynamics

ABSTRACT

In this study, the implementation of a high-order spatial discretization method into a Finite Volume solver is presented. Specific emphasis is put on the analysis of the performance over selected turbomachinery test cases. High-order numerical discretization is achieved by adopting the cell-centered Least-Square reconstruction, which is implemented in the in-house solver HybFlow. The validation of the adopted methodology is performed by assessing the solution of a turbulent flat plate with zero pressure gradient, using a eddy-viscosity transitional model. The test case also evidences the effect of the discretization of gradient-based source terms when a high-order reconstruction methodology is used. In the second part of the paper, the solver is used for the solution of relevant two-dimensional turbomachinery test cases, assessing the impact of 2^{nd} and 3^{rd} order reconstruction on the prediction of the aerodynamics and the heat transfer for respectively a low-pressure blade and a high-pressure turbine vane. It is shown how a high-order reconstruction allows for obtaining a better prediction of turbomachinery aerodynamics, with lower number of elements. The benefits over heat transfer predictions in high Reynolds number conditions are instead limited to the reduction of heat transfer coefficient spikes in under-resolved regions of the blade. Eventually, the methodology is validated for a three-dimensional low-pressure turbine cascade with realistic boundary layer inflow conditions.

1. Introduction

The development of fast and reliable Computational Fluid Dynamics (CFD) solvers is of paramount importance for the analysis of industrial flows such as those arising in the turbomachinery field. To this end, the introduction of high-order methods has become increasingly popular over the last 2 decades for the potential time and memory savings associated with the exploitation of coarser meshes to achieve the desired level of solution accuracy. Over this time, many high-order discretization methods have been introduced and developed, most notably in the context of Discontinuous Galerkin, Spectral Difference and Spectral Elements solvers. Examples of their applications in the turbomachinery community can be found in the works by [9] and [10]. On the other hand, Finite Volume (FV) solvers proved to be reliable in high Reynolds and high Mach numbers regimes thanks to their ability to efficiently manage very complex geometries (typically arising from industrial applications) and possessing shock-capturing ability. Despite this, the level of effort dedicated to the development of FV solvers has been somehow limited. The development of high-order, FV methods started

* Corresponding author.
E-mail address: simone.salvadori@polito.it (S. Salvadori).

https://doi.org/10.1016/j.heliyon.2024.e36478
Received 13 April 2024; Received in revised form 12 July 2024; Accepted 16 August 2024

Available online 22 August 2024

from the work of [5] and has seen further development later in the works of [30], [16], [20]. High order discretization schemes can be achieved by fitting cell variables using piece-wise polynomials of order k to reach a k+1 order of accuracy of the solver. This does not introduce any internal degree of freedom in the cell independently from the discretization order used. One of the first class of k-exact schemes was introduced in [28], where a constrained Least Square (LSQ) procedure is used to obtain polynomials' reconstruction coefficients. The constraint imposed during the LSQ procedure assures that the reconstruction polynomials allow to recover the cell volume averaged quantity. While the method has gained some level of popularity, some improvements have been published over the last years in order to achieve fast convergence rates (as in [26]) and management of highly stretched grids (as in [29]). A second class k-exact schemes, based on a compact reconstruction stencil was introduced by [16], where a successive derivative correction is used to increase the order of accuracy of cell reconstruction, while directly accessing variables (and their derivatives) only in the direct reconstruction stencil of a cell. The advantage with respect to the LSQ based reconstruction is the easiness of implementation, especially for highly scalable solvers, where the communication cost to access cells in large reconstruction stencil can become relevant. Further developments of the method can be found in the paper by [33], with the introduction of Green-Gauss based reconstruction, both for the derivative calculation and correction, along with a single-point quadrature formula for flux computation. While both methods converge at the nominal order (k+1), their direct applications have been somewhat limited. Applications to the solution of inviscid and laminar flows can be found in [30], [20], [25]. In more recent works, the same methods have seen applications to the solution of both steady and unsteady RANS equations as in [33], [21] especially for external aerodynamics. On the other hand, the application of high-order discretization schemes to turbomachinery applications has seen limited popularity. As a matter of fact, in most of the applications of high order methods in the turbomachinery field regards especially Discontinuous Galerkin solvers like in [7], [6], [40], [15] to cite the most relevant ones, where high-order methods have been successfully applied to the study of both turbine vanes and blades aerodynamics. Despite this, to the authors knowledge very limited works have been devoted to the study of high Reynolds number turbomachinery flow, with emphasis on heat-transfer predictions along with the aerodynamics. For this reason, in the present paper we mainly focus on the implementation and the analysis of a LSQ based high-order reconstruction into a FV solver for the solution of turbomachinery test cases using RANS. In fact, in despite of the fact that high-fidelity methods such as Large-Eddy Simulation (LES) would guarantee an accurate analysis of turbulent structures up to the inertial scales, RANS can efficiently predict a large range of complex turbulent flows in turbomachinery applications with limited computational effort and is considered to be suitable for verifying the actual order of accuracy of the solver. Both low/high Reynolds number computations are addressed, with emphasis on the prediction of blade's aerodynamics, heat transfer and losses. The discussion starts with a presentation of the solver, introducing the high-order reconstruction methods, the flux computation and the steady solver characteristics. Section 3 describes the turbulence models selected for the analysis. In Sec. 4.1, the solver is validated against the available experimental data for the transitional flow solution over a flat plate in incompressible regime, where the impact of source terms implementation in a high-order framework is analyzed. In Sec. 4.2, the solver is applied to the solution of a low-pressure high-lift rotor blade to study the effect of high-order discretization over the load and wake losses predictions, in the presence of a laminar separation bubble (LSB). The study for the heat transfer over a high-pressure turbine vane undergoing transition for two different inlet turbulence intensity levels is presented in Sec. 4.3. Eventually, the methodology is extended to a three-dimensional linear low-pressure turbine cascade with realistic inflow conditions in Sec. 4.4, assessing the prediction of the secondary losses using higher order reconstruction. In Sec. 5 the most relevant results of the paper are summarized and possible further improvements are enlisted.

2. Finite volume solver

2.1. Governing equations

HybFlow is a FV solver that adopts a conservative form of the Navier-Stokes equations

$$\frac{\partial \mathbf{w}}{\partial t} + \nabla \cdot (\mathbf{F(w)} - \mathbf{Q}(\mathbf{w}, \nabla \mathbf{w})) = 0 \tag{1}$$

where $\mathbf{w}$ denotes the set of conservative variables $(\rho, \rho\mathbf{u}, \rho e)$, $\mathbf{F(w)}$ denotes the sum of inviscid fluxes and $\mathbf{Q}(\mathbf{w}, \nabla\mathbf{w})$ denotes the viscous fluxes. NS equation is loosely coupled to turbulence transport equations, for which an additional set of equations for transported scalars is solved.

2.2. Reconstruction method

The present solver features high-order (up to the 4th) reconstruction of flow variables within the cells. In the solver, high order variables reconstruction is achieved by means of a constrained Least Square (LSQ). The starting point of the method is a Taylor series expansion of the flow variables about the center of the control volume:

$$\mathbf{w(x)} = \mathbf{w}|_{\mathbf{x}=\mathbf{x}_\alpha} + \sum_{j=1}^{k} \frac{1}{j!} \sum_{i_1 \dots i_j=1}^{d} \frac{\partial w}{\partial x_{i_1} \dots x_{i_j}} (x_{i_1} - x_{\alpha,i_1}) \dots (x_{i_j} - x_{\alpha,i_j}) \tag{2}$$

In Eq. (2), d represents the dimension of the problem, k is the order of the reconstruction polynomial and α is the reference cell for which variables are reconstructed. In order to obtain high order approximation of variables derivatives, it is necessary to access large reconstruction stencils. Both the geometrical characteristics and the variables need to be available upon completing the reconstruction. The dependency of the reconstruction stencil on the order of discretization is shown in Fig. 1, where the reconstruction stencils used in

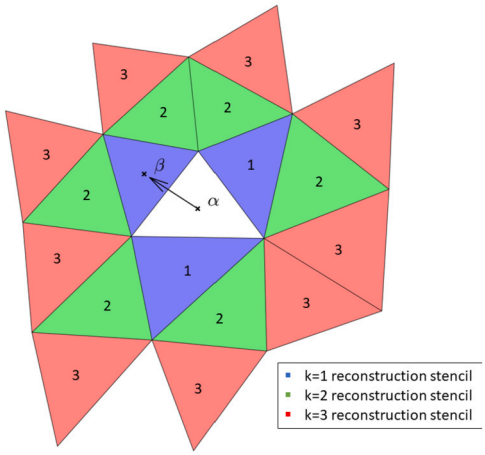

Fig. 1. Reconstruction Stencil.

this work for the computation of high order derivatives are introduced. The first method was proposed by [28], where the polynomial reconstruction is achieved by minimizing the reconstruction error over the neighboring reconstruction stencil, using a Least Square Approach. The reconstruction error over each cell in the reconstruction stencil, can be expressed as:

$$E_{\alpha,\beta} = \frac{1}{V_\beta} \int_{V_\beta} \left(w_\alpha(\mathbf{x}) - \overline{w}_\beta \right) dV \tag{3}$$

where $E_{\alpha,\beta}$ is the reconstruction error of the variable w_α in the 'α' cell, over the volume V_β of the 'β' cell. The minimization problem over the whole reconstruction stencil can be then rewritten in the following form:

$$\mathbf{WAy} = \mathbf{Wb} \tag{4}$$

where $\mathbf{W}$ is a weighting matrix with $\mathrm{W}_{ij} = \frac{1}{|\mathbf{x}_i - \mathbf{x}_j|^p}$, which is introduced to reduce the dependency of solution reconstruction on volume average values of the furthest control volumes in the reconstruction stencil, $\mathbf{y}$ is the vector of variables derivatives ($\frac{\partial w}{\partial x_{i_1} \dots x_{i_j}}$) and $\mathbf{b}$ is the vector of variables volume average. The matrix A accounts for cell geometry and centers' positions and can be pre-computed at the start of the simulation to obtain the reconstruction coefficients for each cell in the domain. The value of p is typically taken between 0 and 2, where 0 corresponds to an unweighted LSQ problem, while more common values are 1 and 2. The latter is the original weighting exponent proposed in [28]. In this case, a value of 1 was chosen according to the analysis performed in [24]. In the present paper, the LSQ approximate solution is obtained by means of the Penrose-Moore pseudo-inverse matrix, obtained by means of a QR factorization of the matrix A. The LSQ matrix is characterized by very high condition numbers in the case of stretched, irregular grids, typical of hybrid meshes composed of tetrahedral and prismatic elements. This problem can be alleviated either by increasing the reconstruction stencil as suggested initially by [5], or by applying a column-scaling preconditioning to the matrix.

2.3. Flux computation

High order computation of the fluxes is based on high order reconstruction of the state variables and their gradients at the cells' face. In order to achieve the desired order of accuracy, the integration of the flux is performed using common Gauss quadrature formulas, where the number of points and the weights are determined based on the requested level of accuracy. As far as the inviscid fluxes are concerned, the high order reconstruction at quadrature points is used in conjunction with the approximate Riemann solver by [34]. On the other hand, the evaluation of the viscous fluxes requires the definition of an intermediate state and an intermediate gradient at the cell face $\mathbf{Q}(\mathbf{w}, \nabla\mathbf{w}) = \mathbf{Q}(\mathbf{w}^*, \nabla^*\mathbf{w})$. The intermediate state is simply taken as the average between the left and right cell values. The intermediate gradient is computed using an average gradient from the cell center, plus a relaxation term. The value of η is set equal to 1 following [29].

$$\mathbf{w}^* = \frac{1}{2}(\mathbf{w}_L + \mathbf{w}_R) \tag{5}$$

$$\nabla^*\mathbf{w} = \frac{1}{2}(\nabla\mathbf{w}_L + \nabla\mathbf{w}_R) + \eta \frac{\mathbf{w}_R - \mathbf{w}_L}{\mathbf{x}_R - \mathbf{x}_L} \tag{6}$$

2.4. Non-linear solver

The steady solution of the non-linear set of equations is found by means of iterative relaxed Newton method and a pseudo-time marching technique which relaxes the non linear solver. The method attempts to solve the non-linear system of equations using the following iterations.

$$\mathbf{w}^{i+1} = \mathbf{w}^{i} - \left(\frac{\partial \mathbf{R}}{\partial \mathbf{w}}\right)^{-1} \mathbf{R}\left(\mathbf{w}^{\mathbf{n}}\right) \tag{7}$$

In order to accelerate convergence after the initial non-linearities have been dissipated, it is possible to adapt the CFL value according to the residual drop. While some authors adopted very complex local time stepping adaption techniques (e.g. [39] [18]), in the present work, the authors adopted a constant CFL value.

The Newton iteration requires the evaluation of the residuals Jacobian. To this end, there are two different possibilities: compute an exact Jacobian or use an approximate Jacobian. In the present version of the solver the second choice was adopted, which is easily extendable to any type of turbulence model and is state of the art in most of the solvers. As pointed out by [26], when high-order reconstruction schemes are used, the construction of the Jacobian should take into account the perturbation of the solution in all the cells which are part of the reconstruction neighborhood. Despite this, the method has a twofold drawback: on the first hand, the higher is the discretization order, the larger is the size of the linear system to be solved. The second drawback is that the formula requires various computationally intensive passages, whose cost augments as far as the reconstruction cells are increased. In the present work, the approximate Jacobian is based simply on a 1^{st} order finite difference approximation. Namely, only the variation of the cell average value is considered, while the effect of the perturbation over the gradients is discarded. When the perturbation method is used, the choice of the perturbation value needs to be careful. As a matter of fact, the perturbation needs to be small in order to give a good representation of residuals derivatives, but it cannot be too small as to introduce round-off errors.
In the present implementation, the perturbation is constant for flow variables, equal to 10^{-3}, while the following rule is used for turbulence variables (Q_i):

$$\epsilon_{turb} = max(\epsilon_{min}, \epsilon_{rel} \times Q_i) \tag{8}$$

The values of ϵ_{min} and ϵ_{rel} are chosen respectively equal to 10^{-8} and 10^{-6}. Once the Jacobian is computed, the linearized system of equations needs to be solved. To this end, a parallel GMRES ([35]) algorithm, with a Schwarz additive right preconditioner [39], is used. The latter has been chosen for its simplicity in the implementation, especially in parallel environment. As a matter of fact, the construction of the preconditioner is sequential and does not need any additional communication between processors. The additive Schwarz method, is part of a class of domain decomposition methods which allows the solution of linear system of equations. Despite being rather inefficient as solvers, especially when the number of subdomains increases, Domain Decomposition methods work quite well when used as preconditioners to more robust linear solvers such as the GMRES. In order to build the one-level Schwarz preconditioner, a series of subdomains is created at the start of the simulation by means of a k-way algorithm. Defining R_i as the vector which maps the global domain to local subdomains, the corresponding local preconditioner (S_i) and the global preconditioning matrix (S), can be obtained as:

$$A_i = R_i A R_i^T \tag{9}$$

$$S_i = R_i^T A_i^{-1} R_i \tag{10}$$

$$S = \sum_{i=1}^{N_{sub}} S_i \tag{11}$$

The formation of the preconditioner, requires to perform the inversion of the local subdomain matrix A_i. Rather than performing an expensive exact inversion of the matrix, A_i^{-1} is approximated by means of a ILU(0) factorization. Despite higher levels of fill-in have been used in the literature, the choice is case dependent, therefore the economic ILU(0) has been used. The stopping criteria for the linear system solution was based on residuals dropping by at least two orders of magnitude. A maximum number of 100 Krylov sub-vectors was enforced.

3. Turbulence model

Turbulence closures based on the eddy-viscosity assumption are implemented in CFD solvers using two transport equations, one for the turbulent kinetic energy k and one for a dissipation rate parameter (i.e., ω, see [38]). These approaches are fully-turbulent and are not able to predict boundary layer transition from the laminar to the turbulent state even in baseline cases. That limitation can be overcome either by using scale-resolving approaches such as wall-resolved LES or by considering physics-based additional parameters that can mimic the transition mechanism. The authors decided to use the latter approach, being the high computational cost of LES not justified by the aim of the present paper that is the validation of a high-order spatial discretization method for a finite-volume solver.

The turbulence model adopted for the present activity is the $k - \overline{v^2} - \omega$ by [23]. The model variables account for total fluctuation energy k, small scale, three-dimensional velocity fluctuations $\overline{v^2}$ and a length scale variable ω. The additional turbulent transport equations in incompressible form are here reported:

Table 1
Transition model coefficients.

$A_0 = 4.04$	$C_{INT} = 0.95$	$C_{\omega 1} = 0.44$
$A_s = 2.12$	$C_{TS,crit} = 1000$	$C_{\omega 2} = 0.92$
$A_v = 3.8$	$C_{R,NAT} = 0.02$	$C_{\omega R} = 1.15$
$A_{BP} = 0.2$	$C_{l1} = 3.4{*}10^{-6}$	$C_\lambda = 2.495$
$A_{NAT} = 200$	$C_{l2} = 1.0{*}10^{-10}$	$\beta^* = 0.09$
$A_{TS} = 200$	$C_R = 0.32$	$Pr_\theta = 0.85$
$C_{BP,crit} = 1.5$	$C_{\alpha,\theta} = 0.035$	$\sigma_k = 1$
$C_{NC} = 0.1$	$C_{SS} = 3.0$	$\sigma_\omega = 1.17$
$C_{NAT,crit} = 1450$	$C_{\tau,l} = 4360$	$\sigma_{\omega 2} = 1.856$

$$\frac{Dk_T}{Dt} = P_k - D_k - min(\omega k, \omega\overline{v^2}) + \frac{\partial}{\partial x_j}\left[\left(\nu + \frac{\alpha_T}{\sigma_k}\right)\frac{\partial k}{\partial x_j}\right] \tag{12}$$

$$\frac{D\overline{v^2}}{Dt} = P_{\overline{v^2}} + R_{BP} + R_{NAT} - \omega v^2 - D_{\overline{v^2}} + \frac{\partial}{\partial x_j}\left[\nu + \frac{\alpha_T}{\sigma_k}\frac{\partial \overline{v^2}}{\partial x_j}\right] \tag{13}$$

$$\begin{aligned}\frac{D\omega}{Dt} =& P_\omega + \left(\frac{C_{\omega R}}{f_W} - 1\right)\frac{\omega}{\overline{v^2}}\left(R_{BP} + R_{NAT}\right) - C_{\omega 2} f_w^2 \omega^2 + \\ & 2\beta^*(1 - F_1^*)\sigma_2 \frac{1}{\omega}\frac{\partial k}{\partial x_j} + \frac{\partial \omega}{\partial x_j}\frac{\partial}{\partial x_j}\left[\left(\nu + \frac{\alpha}{\sigma_\omega}\right)\frac{\partial \omega}{\partial x_j}\right]\end{aligned} \tag{14}$$

The transition process is controlled by means of the terms R_{BP} and R_{NAT}, which are activated to model by-pass and natural transition mechanism, respectively. The terms P and D respectively control the production and destruction of the turbulence variables. The latter is necessary to damp near-wall fluctuations. While a comprehensive description of the model is present in the referenced article, some remarks regarding its final implementation will be presented. The full set of transition model constants is available in Table 1. The turbulence model is implemented in its compressible form. To this end, equations are modified by transporting $\rho k, \rho\overline{v^2}$ and $\rho\omega$ and multiplying the right-hand side of the equations by the local flow density. Moreover, the compressible version of the Reynolds stress tensor is adopted:

$$\tau_{ij} = \mu_T\left(2S_{ij} - \frac{2}{3}\frac{\partial u_k}{\partial x_k}\delta_{ij}\right) - \frac{2}{3}\rho k \delta_{ij} \tag{15}$$

Considering the variable reconstruction order of the present Finite-Volume solver, care must be taken in the definition of the source terms in the equations. As a matter of fact, similarly to other eddy-viscosity based turbulence models, the $k - \overline{v^2} - \omega$ makes use of the Boussinesq approximation to account for the Reynolds stresses. The latter is then dependent on the definition of average (in the volume sense) of velocity gradients, through the flow strain S. Moreover, the model destruction terms D_k and $D_{\overline{v^2}}$ are respectively defined as:

$$D_k = 2\nu\frac{\partial\sqrt{k}}{\partial x_j}\frac{\partial\sqrt{k}}{\partial x_j} \qquad D_{\overline{v^2}} = 2\nu\frac{\partial\sqrt{\overline{v^2}}}{\partial x_j}\frac{\partial\sqrt{\overline{v^2}}}{\partial x_j} \tag{16}$$

which depend on the gradients of $\sqrt{k}$ and $\sqrt{\overline{v^2}}$. The current implementation of the model exploits the LSQ reconstruction procedure for all flow and turbulence variables. As far as the $\sqrt{k}$ and $\sqrt{\overline{v^2}}$ are regarded, the cell averaged values are obtained from a point-wise conversion of the value of k and $\overline{v^2}$. Upon computing cell-centered velocity and turbulence gradients, one possible strategy for the computation of source terms is to directly use them. This means that the LSQ method is used both for reconstruction purposes and for the computation of source terms. Despite this, as suggested by [2], the ability of the LSQ reconstruction to yield correct predictions of the cell-center gradients depends on the weighting, especially on highly stretched grids. This could lead to a worse definition of volume average gradients adopted in the source terms. For this reason, in the present activity, the use of the LSQ reconstruction based gradients, will be compared to a second approach based on the of Green-Gauss theorem (Eq. (17)):

$$\nabla U_j = \frac{1}{V_j}\int_{\partial V_j} U_j \mathbf{dS}\cdot\mathbf{n} \tag{17}$$

where **dS** is cell surface element and **n** is the normal vector. The surface integral of the flow variables is computed using the same Gauss quadrature rules employed for flux computations as in Eq. (18):

$$\int_{\partial V_j} U_j dS = \sum_{i=1}^{N_{face,j}}\sum_{k=1}^{N_{quad}} U_{ik} \times w_{ik} \tag{18}$$

Table 2
Flat plate - Mesh characteristics.

Mesh	N_{DOF}	y^+
M1	7128	≈ 3.0
M2	15617	≈ 1.5
M3	33654	≈ 0.75
M4	96720	≈ 0.38

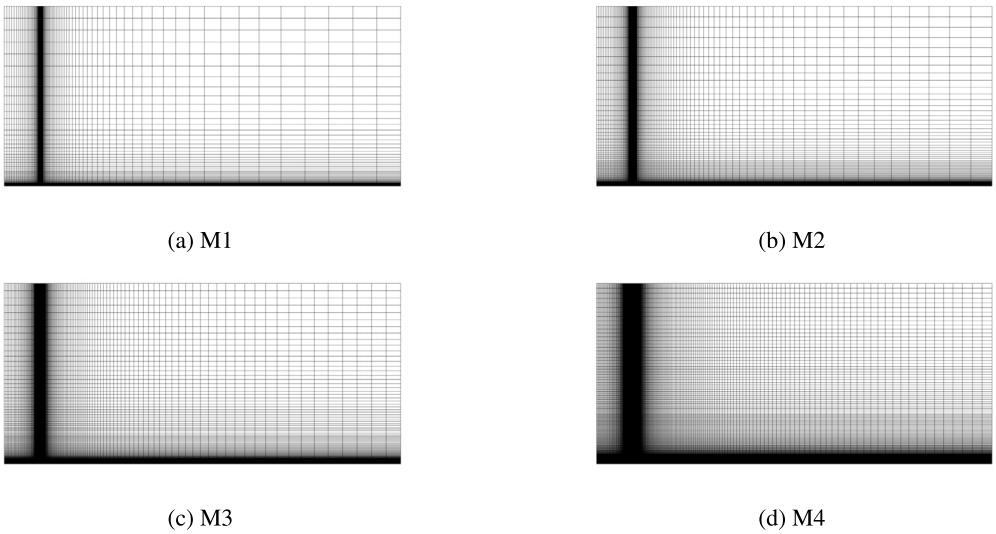

(a) M1 (b) M2

(c) M3 (d) M4

Fig. 2. Flat plate - Mesh details.

where w_{ik} and U_{ik} are the weight and variable value in the $k-th$ quadrature point of the $i-th$ face, respectively. The face value U_{ik} is computed as the arithmetic mean of the left and right LSQ reconstruction of U in the quadrature point as in Eq. (19).

$$U_{ik} = \frac{U_{ik}^{-} + U_{ik}^{+}}{2} \tag{19}$$

4. Results

In this section, the implemented high-order method is applied to the solution of NS equations arising from three different applications. The first test case is the transitional flow over a flat plate with zero pressure gradient, namely the T3A and T3B cases of the classic ERCOFTAC database ([12]). The second and the third test cases refer to the study of two-dimensional airfoils, representing the T106C low-pressure turbine blade and the LS89 high-pressure turbine vane, respectively. The last test case is the low-pressure turbine blade T106A, which represents an extension of the described methodology to three-dimensional computations.

4.1. Transitional flow over flat plate

The first test case for validation of the solver is the transitional flat plate with zero-pressure gradient that can be retrieved from the classic ERCOFTAC database. In the model setup, symmetry planes were applied upstream of the plate LE and over the upper surface. Structured meshes were used for the simulation of the flow field, clustered in the LE region of the plate and over the viscous wall. All the meshes have been generated using the commercial mesh generator Centaur^{TM} [11]. The characteristics of the meshes are summarized in Table 2, which reports the number of degrees of freedom and y^+ for each of the meshes. The latter value reports the case of the T3B setup using the experimental friction velocity u_τ in order to avoid the effect of shear stress prediction on the definition of y^+. The friction velocity is taken in the turbulent region, after transition has occurred, for a value of Re_x =3.82 $\times 10^5$. The meshes are instead visualized in Fig. 2.

The meshes from M1 to M3 have been used to assess the convergence of the skin friction prediction for different reconstruction orders. In particular, second, third and fourth order reconstruction methods have been used. The meshes have been obtained by approximately doubling the total number of degrees of freedom, keeping the same aspect ratio. The last mesh M4, has been run only with a second order reconstruction and has been used to verify solution independence from mesh discretization and reconstruction order. The test cases used for the validation are the T3A and T3B. The boundary conditions mimic the experimental setup in terms of flow velocity and decay of turbulence intensity. The summary of boundary conditions is reported in Table 3. The values of viscosity ratio and turbulence intensity reported in the table refer to the conditions at the LE of the flat plate. The inlet value can be retrieved

Table 3
Flat plate - Boundary conditions.

	T3A	T3B
U [m/s]	5.4	9.4
Tu [%]	3.3	6.5
VR	12.0	100.0

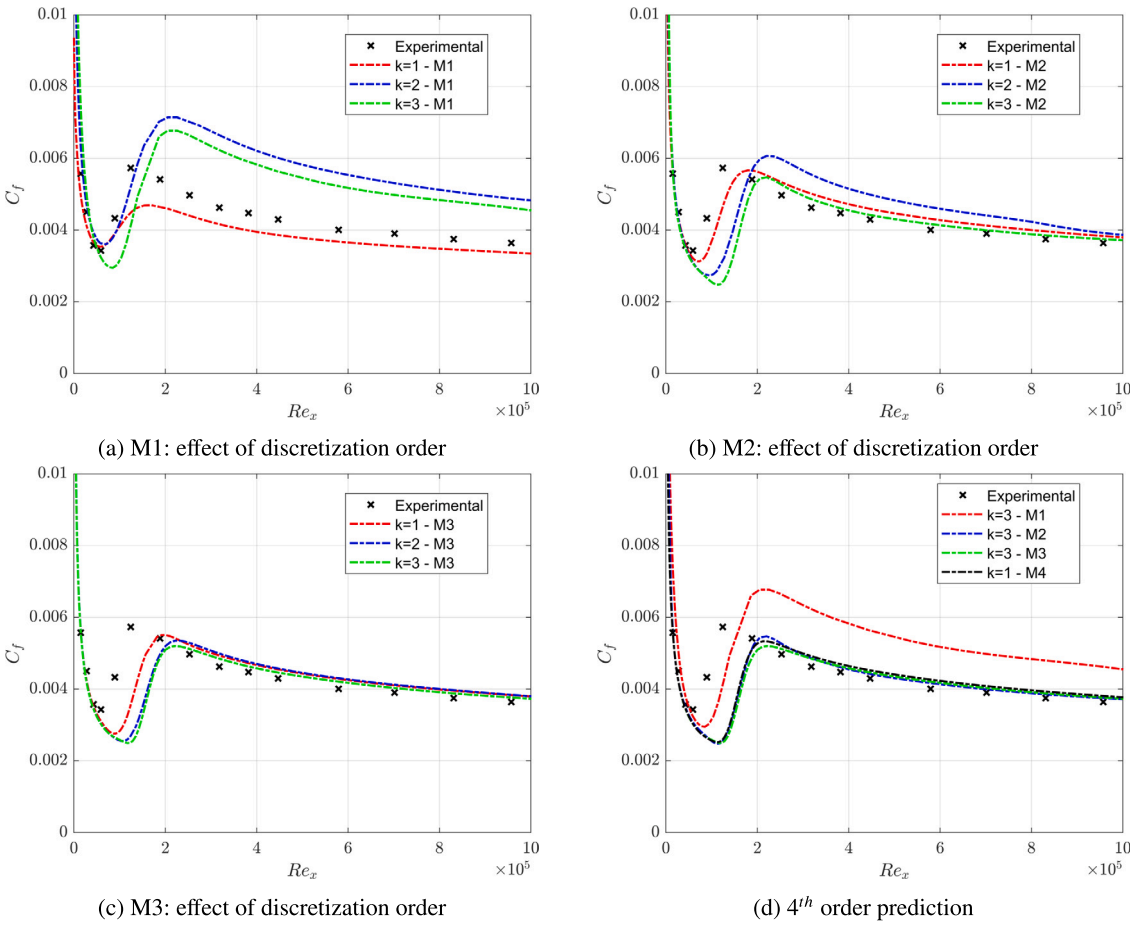

(a) M1: effect of discretization order

(b) M2: effect of discretization order

(c) M3: effect of discretization order

(d) 4^{th} order prediction

Fig. 3. T3B - Skin friction coefficient prediction using LSQ gradients for the computation of source terms.

by integrating the free-stream turbulence decay equations, under constant free-stream velocity U_∞ (Eq. (20) and (21)). The values imposed at the LE have been retrieved from [23].

$$U_\infty \frac{d\overline{v^2}}{dx} = -\omega \overline{v^2} \tag{20}$$

$$U_\infty \frac{d\omega}{dx} = -C_{\omega 2}\omega^2 \tag{21}$$

The T3B case has also been used to assess the effect of source terms discretization on the prediction of the skin friction coefficient. The results obtained using the baricentral value of the flow and turbulence quantities gradients are shown in Fig. 3, where the predictions obtained on the meshes M1-M3 are shown for different the reconstruction order (3a-3c). Fig. 3d reports the comparison between the 4th order predictions with the results of the second order reconstruction obtained on mesh M4. On the coarsest mesh, the implementation of the high order reconstruction has the main advantage to predict the occurrence of the transition process around the correct location, while a relevant over-prediction of the skin friction coefficient in the turbulent region is present both for k = 2 and k = 3. The same process is not correctly predicted at k = 1 which indicates the persistence of an almost laminar flow over the whole plate. For mesh M2, the transition process occurs for all the tested discretization orders. While the transition length (which can be retrieved from the slope of the skin friction coefficient) is predicted correctly for all the values of k, higher order discretizations lead to a later transition onset, compared to k = 1, deteriorating the prediction of the experimental values. For M = 3, the reconstruction

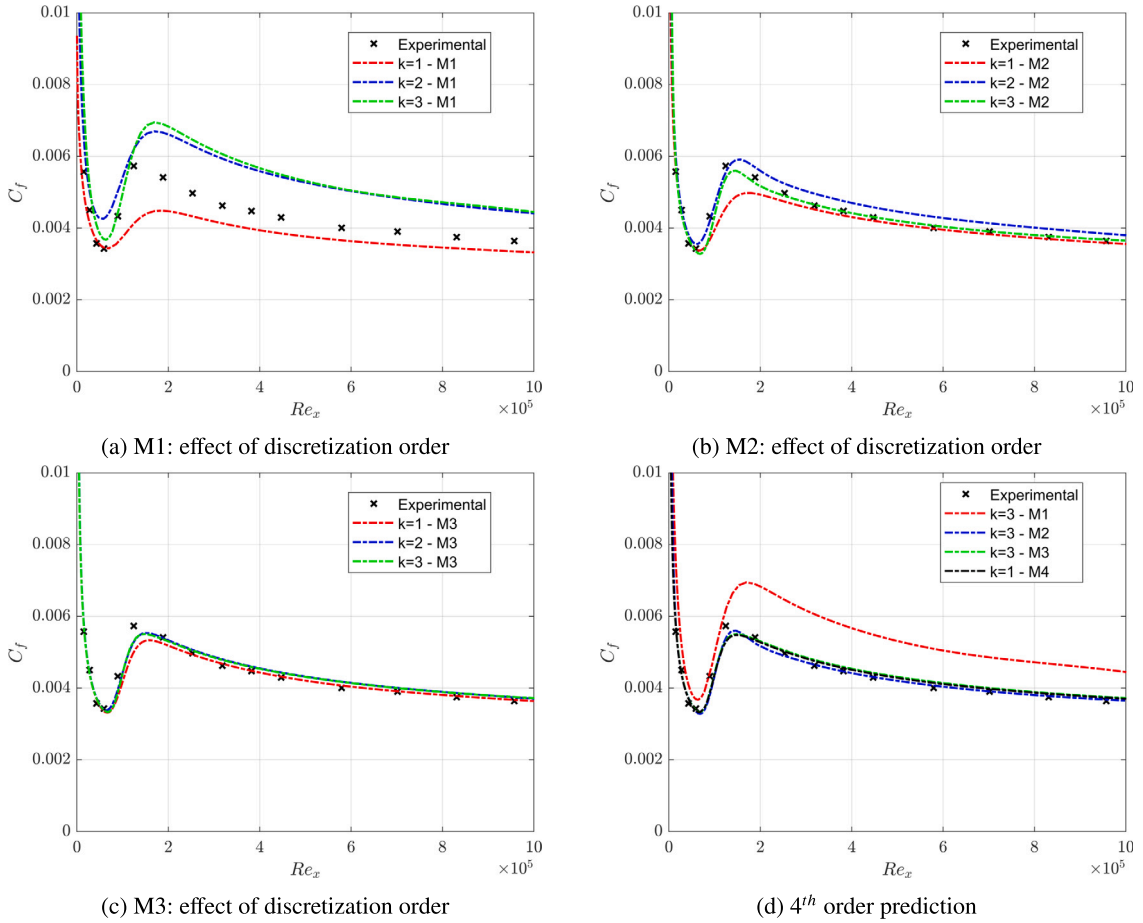

(a) M1: effect of discretization order

(b) M2: effect of discretization order

(c) M3: effect of discretization order

(d) 4^{th} order prediction

Fig. 4. T3B - Skin friction coefficient prediction using Green-Gauss theorem for the computation of source terms.

orders return similar predictions in the fully turbulent region and for k = 2 and k = 3 also the transition onset location. Similarly to coarser meshes, the increase of reconstruction order delays the transition onset. In Fig. 5d, the fourth order predictions are compared with the second order predictions obtained on mesh M4. Most notably, numerical values obtained on coarser meshes converge to the same results as the finest mesh, which features roughly 3× and 6× the degrees of freedom of meshes M2 and M3 respectively. Wrong predictions are obtained for M1 instead, indicating an insufficient geometrical discretization in the transition region. Eventually it is seen that while the predictions of the skin friction coefficient correctly converge towards the same result when the reconstruction order/mesh density is increased, the use of central values of gradients leads to a delayed transition onset.

A secondary set of simulations was run by discretizing the source terms using average gradients from the application of the Green-Gauss theorem. The results are shown in Fig. 4. Similarly to the LSQ computation, the first three figures compare the solutions obtained on the same mesh for different reconstruction orders with experimental values. The last figure is used to assess solution convergence. Starting from mesh M1, the change of the strategy for the computation of the source terms confirms the results already discussed in Fig. 3. As a matter of fact, for k = 1 the skin friction coefficient is underestimated. At higher orders, instead, the transition onset position is correctly predicted, and the two simulations retrieve the same value in downstream of the end of transition point. For k = 2, the skin friction at the transition onset is overestimated (25% higher than the experimental value), while a better prediction is found for k = 3. For mesh M2, a better prediction of the transition process is obtained for the 2^{nd} order discretization compared to M1, while a very good agreement between numerical results and experiments is found for k = 3. The skin friction at the end of transition is slightly underestimated as CFD predicts a value of $C_f \approx 5.5 \times 10^{-3}$, while the experimental measurement shows $C_f \approx 5.7 \times 10^{-3}$. The transition length is correctly predicted as well as the skin friction in the fully turbulent region. For mesh M3, the numerical results have almost converged both in terms of spatial discretization and flow reconstruction. For k = 1, the predicted transition length is higher compared to k = 2 and k = 3, which feature the same skin friction coefficient trend. In Fig. 4d, the $4th$ order results comparison with the predictions obtained for k = 1 on M4, confirm the goodness of the approach in reproducing flow transition. M1 still represents a too coarse mesh for the prediction of the transition process, while only minor differences exist in the predictions at the 4^{th} order between M2 and M3.

The last set of simulations runs for the flat plate test case, reproduces the experiments of the T3A run. The results are presented in Fig. 5. The lower turbulence intensity of this test case leads to a higher transition length ($Re_x \approx 7 \times 10^4$), which makes it useful

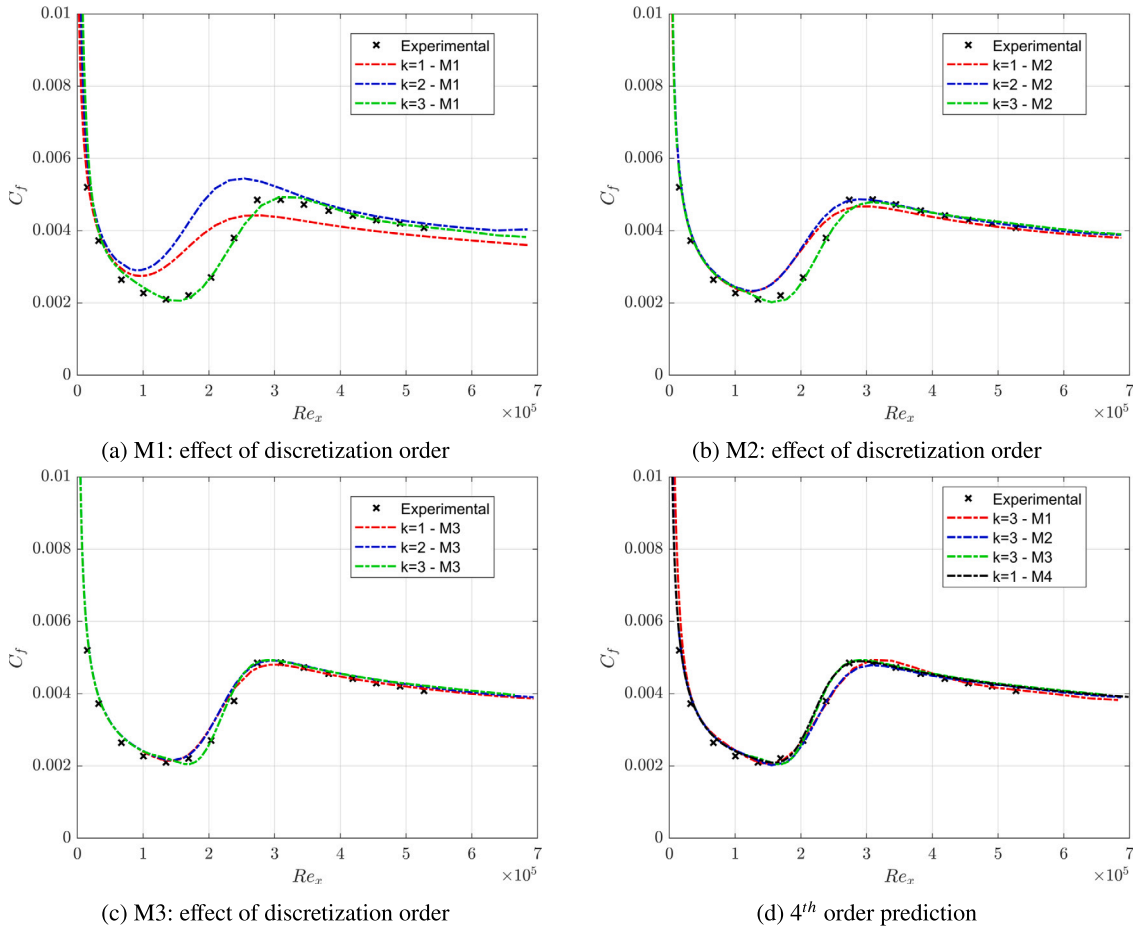

(a) M1: effect of discretization order

(b) M2: effect of discretization order

(c) M3: effect of discretization order

(d) 4^{th} order prediction

Fig. 5. T3A - Skin friction coefficient prediction using Green-Gauss theorem for the computation of source terms.

to assess the effect of high order discretization in the case of lower flow gradients in the streamwise direction. On the coarsest mesh (Fig. 5a), the effect of the discretization order is now even stronger. Similarly to the T3B test case, for k = 1, the transition process is slow and the fully turbulent value of the skin friction coefficient is under-predicted. Increasing the discretization order to k = 2, the transition onset position is not affected, remaining upstream of the experimental one, but now transition is completed with the correct slope. For k = 3 instead, the transition onset is correctly captured, while the transition length is only slightly overestimated. Differently from the T3B test case, the 4^{th} order reconstruction already provide reasonable agreement with the experimental values. The same trend is shown in Fig. 5b, where for k = 3 the agreement with the experimental values is remarkable. On the other hand, for k = 1 and k = 2, the transition onset occurs downstream of the one predicted on mesh M1, but the experimental transition length is overestimated. For mesh M3, the different discretization orders predict very similar values. The transition onset point still moves downstream at k = 3, while the same skin friction coefficient is predicted after the end of transition. Similarly to coarser meshes, for k = 1, the skin friction coefficient is lower, even though much closer to the predictions at high order. In Fig. 5d all the results at k = 3 are compared, with the second order predictions on mesh M4. It must be noted that for k = 3, the predictions on meshes M1 and M2, there is still a slight variation compared to the results on M3 and M4, at the end of the transition process. This is adduced to the fact that meshes are clustered around the LE of the flat plate, so mesh gets coarser at higher Re_x values. For the T3A case, the prediction of the transition onset and length, requires a value of x^+ approximately between 250 (at the onset) and 650 (at the end of transition). These values are achieved using a fourth order reconstruction for the mesh M3. Conversely, for a second order computation, the value of x^+ necessary to achieve a mesh independent solution varies between 150 and 400. For the T3B test case, the required streamwise spacing x^+ is approximately 125 at the transition onset and 350 at the end of transition. These values correspond to roughly twice the dimensions of the mesh M4.

The total cost of the simulations is reported for the T3B test case in Table 4. The cost refers to simulations using a constant CFL number equal to 10.0, stopped when the residuals drop below 5×10^{-10}, which is a limit achieved by all simulations, regardless of the mesh discretization and the reconstruction order. All high-order simulations are restarted from lower order ones, so the cost reported refers to the full chain to achieve a converged solution. It is shown that the fourth order simulation achieves the same predictions as the fine mesh but with an approximate reduction of the total convergence time by a factor of 4.

Table 4
T3B non-dimensional convergence time.

	k=0	k=1	k=2	k=3
M1	0.0058	0.0100	0.0129	0.0169
M2	0.0285	0.0468	0.0607	0.0730
M3	0.1295	0.1953	0.2267	0.2553
M4	0.7819	1.0	-	-

Table 5
T106C blade characteristics.

c [mm]	93.01
c_{ax} [mm]	79.97
β_1	32.7
$Ma_{2,is}$	0.65
$Re_{2,is}$ [*10^3]	[80:250]
Tu [%]	0.8
ILS [mm]	30

Table 6
T106C - Mesh characteristics.

Mesh	N_{DOF}	y^+	$N_{profile}$
M1	14760	<1	231
M2	44656	<1	440
M3	80516	<1	513

As a final remark, it must be said that the present predictions of the skin friction coefficient are in accordance with the ones presented in [23], which were obtained using a commercial solver.

4.2. Aerodynamics of low-pressure turbine blade

The T106C is a high-speed, high-lift, low-pressure turbine blade investigated experimentally at the von Karman Institute for Fluid Dynamics. Details of the test case have been reported by [27]. The wake losses have been retrieved from the work of [8]. The profile has been used as benchmark for the validation of turbomachinery solvers as well as transition models ([31,4,37]). The main characteristics of the blade as well as the range of simulated operating conditions are summarized in Table 5. For the selected range of Reynolds number, the profile features a laminar separation bubble in the aft region of the suction side, which both affects the loading distribution and the wake. Similarly to the flat plate test case, the airfoil has been simulated using three different unstructured meshes whose characteristics are summarized in Table 6. The meshes are hybrid, with quadrilateral elements in the wall vicinity and triangular elements in the free-stream region (Fig. 6).

The numerical predictions obtained with the 3 meshes for different for $100,000 < Re_{2,is} < 250,000$ are compared with the experimental measurements in Fig. 7, 8 and 9 using the isentropic Mach number (Eq. (22)) and the outlet total pressure losses. In the range of the simulated Reynolds number, the blade features a laminar separation bubble in the aft region of the suction side. The latter is instead investigated by means of the skin friction coefficient (Eq. (23)).

$$Ma_{is} = \left\{ \left[\left(\frac{P_{01}}{P} \right)^{\frac{\gamma}{\gamma-1}} - 1 \right] \frac{\gamma-1}{2} \right\}^{0.5} \tag{22}$$

$$C_f = \frac{\tau_w}{0.5 \rho_{2,is} U_{2,is}^2} \tag{23}$$

Regardless of the conditions, reconstruction order or mesh, all the simulations fail to predict the isentropic Mach for $X/C_{ax} < 0.4$, most notably at the blade LE. This mis-prediction is common in the literature and is probably to be addressed to the larger inlet flow angle obtained the experimental campaign as suggested by [17], or to 3D effects which are not modeled in the present activity ([19]). At $Re_{2,is} = 100,000$ (Fig. 7), the prediction of the loading obtained using M2 and M3 is in accordance with the experimental values, apart from a small peak in the Mach number evidenced by the measurements at $0.83 < X/C_{ax} < 0.85$. On other hand, the coarsest mesh overestimates the velocity peak at $X/C_{ax} \approx 0.6$ when a second order reconstruction is employed. Further downstream the pressure recovery is instead faster compared to the experiments, indicating that the reattachment of the separation bubble has occurred. For k=2, the predictions of the loading using M1 improve. The velocity peak is reduced from 1.34 to 1.32, and the pressure recovery for $X/C_{ax} > 0.85$ correctly matches experimental measurements. The different predictions of the loading between k=1 and k=2 on M1, are due to the different structure of the separation bubble, which can be inferred from the skin friction coefficient shown in Fig. 7c and 7d. On the coarsest mesh, the second order simulation predicts a later separation ($S/S_0 \approx 0.6$) and a reattachment point at $S/S_0 \approx 0.9$ compared to all the other cases. All the other simulations instead predict an open bubble, which explains the

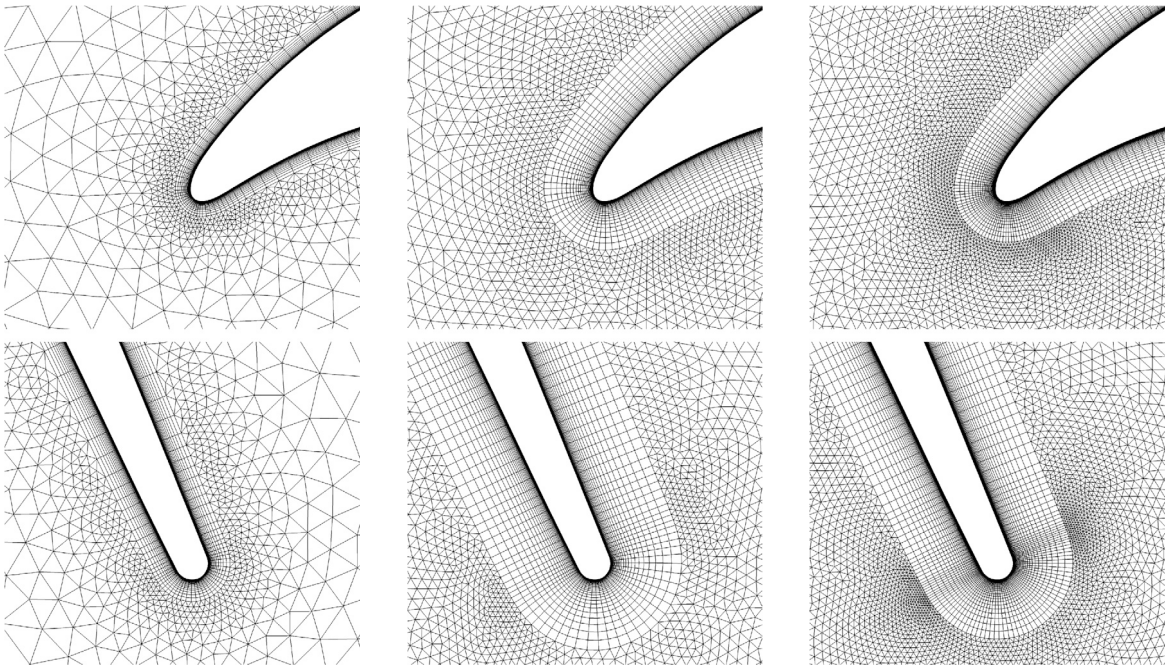

Fig. 6. T106C - LE and TE mesh details.

slower pressure recovery evidenced in loading plot and their better match with the experimental results. At k = 2, M1 simulation also predicts an open separation bubble, while a fully converged solution in terms of skin friction coefficient is found using M3, which shows the same behavior of C_f, both at k = 1 and k = 2. The intermediate mesh predicts the same separation point location as M3, but only the third order reconstruction achieves a similar distribution of the skin friction coefficient in the separated region of the flow up to the recovery point ($S/S_0 \approx 0.85$), with a small overestimation of C_f (2×10^{-4}) in the recovery region compared to M3. The change in the prediction of the separation bubble also affects the wake distribution. The losses predicted at the outlet measurement plane are highly underestimated due to the very coarse mesh. The peak in the losses increases using the third order discretization due to the prediction of the open separation bubble. On the other hand, M2 and M3 overestimate the pressure deficit, while the spread is underestimated. It must be said that this type of behavior is common in eddy-viscosity based transition models as shown by [1]. The effect of higher order reconstruction is instead limited. As a matter of fact, k = 2 simulations return similar values to the corresponding k = 1 simulations.

At $Re_{2,is} = 160{,}000$, the predictions are similar to the case at $Re_{2,is} = 100{,}000$. The most notable differences regard the loading and the wake. As far as the former is considered, once again, the second order computation on the coarse mesh predicts the fastest pressure recovery for $X/C_{ax} > 0.85$, which is again related to the fast reattachment of the separation bubble (see also Fig. 8c and 8d). This behavior leads to a better match with the experimental results. All the other cases tend to underestimate the pressure recovery, probably due to a slight mis-prediction in the separation bubble size. As far as the wake is concerned, Fig. 8b shows that, while an overestimation of the deficit still exists in the center of the wake (≈ 1% of the inlet total pressure), the spreading of the wake is properly predicted, especially at k = 3, which slightly shifts the pressure deficit towards lower pitchwise coordinates.

Eventually at $Re_{2,is} = 250{,}000$, the simulations predict the same shape of the M_{is} (Fig. 9a), indicating that the shape of the separation bubble is no longer discriminating the distribution of the pressure over the suction side. All the simulations predict the recovery point too downstream ($X/C_{ax} \approx 0.82$ in the experimental setup and $X/C_{ax} \approx 0.84$ for the CFD), indicating that the reattachment of the separation bubble is too slow. The distribution of the skin friction coefficient indicates a reattached bubble for all combinations of mesh and order of reconstruction. The coarsest mesh predicts the shortest bubble, reattaching at $S/S_0 \approx 0.84$. For all the other cases, the reattachment point moves to $S/S_0 \approx 0.86$. A fully converged skin friction prediction is predicted only at k = 2, both on mesh M2 and M3. The highest Reynolds also exhibits the best prediction of the wake profile at the outlet measurement plane. While a small over-prediction of the deficit still exists for mesh M3, the wake shape is captured correctly both by M2 and M3 regardless of the reconstruction order. It is noted that the effect of the higher order discretization at low-Reynolds conditions is higher than the effect at high-Reynolds conditions. This is adduced to the fact that the main contribution of the increase of the reconstruction order is in the prediction of the separation bubble size, especially in terms of reattachment position. Contrarily to the low and intermediate Reynolds numbers, at $Re_{2,is} = 250{,}000$ the bubble is smaller in size and prone to reattachment, which makes the effect of higher order reconstruction limited to wall quantities like the skin friction coefficient. For the low and intermediate Reynolds numbers, the streamwise mesh spacing necessary to avoid an anticipated reattachment point increases. In particular, depending on the Reynolds number, meshes M2 and M3 require a value of s^+ of approximately 30-50, respectively. On the other hand for k = 2 and M1, the value

Table 7
T106C non-dimensional convergence time for $Re_{2,is} = 250{,}000$.

	k = 0	k = 1	k = 2
M1	0.0347	0.0431	0.0503
M2	0.0566	0.0939	0.1927
M3	0.5157	0.7903	1.0

Table 8
LS89 characteristics.

Test	MUR237	MUR218
c[mm]	67.647	67.647
β_1 [°]	0	0
P_{out} [bar]	1.179	1.19
$Ma_{2,is}$	0.775	0.760
$Re_{2,is}$ [$*10^3$]	1000	1000
Tu [%]	6	4
VR []	75	50

Table 9
LS89 - Mesh characteristics.

Mesh	N_{DOF}	y^+	$N_{profile}$
M1	12158	<1	250
M2	23027	<1	300
M3	46966	<1	683

of s^+ required increases to 80 at low-Reynolds conditions and is above 100 at intermediate and high Reynolds. It can be concluded that the required mesh spacing is roughly twice as much as the one required by second order methods. The non-dimensional convergence time to achieve a converged solution is reported in Table 7 for the case at $Re_{2,is} = 250{,}000$. The values refer to a constant CFL value equal to 5.0, while the residual threshold is set to 5×10^{-8}. Considering that the high order discretizations of M2 and M3 yield similar results in terms of loading, wake and skin friction coefficient, it can be said that the use of k = 2 reconstruction allows to reduce the overall computational time by a factor of 5.

4.3. Heat transfer for high-pressure turbine vane

The last section is dedicated to the analysis of the heat transfer over the high-pressure turbine vane LS89. The experimental campaign is documented in [3]. In the present activity, the MUR218 and MUR237 test cases have been reproduced. The main operating conditions and geometrical characteristics are reported in Table 8. The turbulence boundary conditions specified in the table refer to the conditions at the LE of the blade, while inlet values are obtained with the same procedure described in Sec. 4.1. For both test cases, the turbulence boundary conditions have been retrieved from a previous numerical campaign performed on the same test case by [36]. Similarly to the low-pressure turbine blade, the LS89 has been simulated using 3 different meshes, with second and third order reconstruction. The characteristics of the mesh are reported in Table 9, while a close-up view of the LE and TE regions is provided in Fig. 12.

The first test case discussed is the MUR218, which is shown in Fig. 10. The experiment run at 4% turbulence intensity shows boundary layer transition after S = 60 mm. Simulations predict a delayed transition onset which occurs at S≈67 mm. The transition point does not depend on the selected mesh or the reconstruction order, as the variability of Nu up to the transition point over the suction side is limited. After the transition onset, the increase in Nu using M1 and M2 is slower than the one predicted on M3, while the same increase is not captured by increasing the reconstruction order from k = 1 to k = 2. On the pressure side, the Nusselt number is well predicted by all the test cases, up to S≈-20 mm, while it is underestimated downstream. The figure also shows a close-up view of the heat transfer coefficient for the coarsest mesh, in the region 10 mm < S/S_0 <25 mm. These highlights how, while the prediction using k = 1 and k = 2 yields similar results on overall, still significant changes can occur in regions of high gradients. As a matter of fact spurious peaks in the Nusselt number arise with k = 1 and M1, which are instead limited by increasing the reconstruction order to k = 2. Fig. 11, shows the predictions on the MUR237 case, which is instead run at Tu = 6%. The increase in turbulence level moves the transition point upstream in the experiments (S≈40 mm). With respect to MUR218, the Nusselt increases over the PS of the blade, while similar levels are reached after the transition process is completed in the aft region of the SS. Simulations are not able to reproduce the increase in the experimental increase in the Nusselt number over the PS, which reaches similar levels of the MUR218 test case. As far as the transition region is considered instead, the onset is predicted at S≈52 mm, evidently delayed with respect to the experimental measurements. Both issues have been found in the analysis performed by [36], where a similar version of the turbulence models was used to study the same test cases. It must be noted that similar mispredictions of the transition point have been reported in other studies (e.g. by [22] and by [13]), where a LES approach was used to tackle turbulence closure. Similarly to Fig. 10,

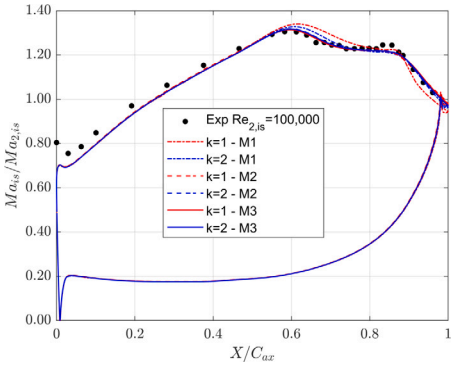

(a) Blade loading

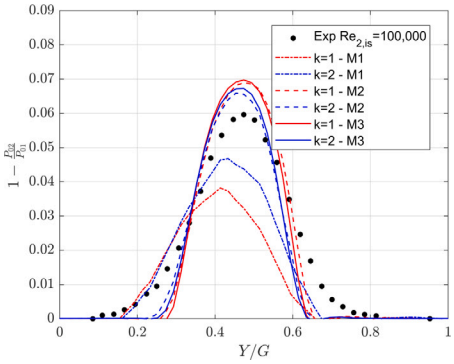

(b) Outlet total pressure losses

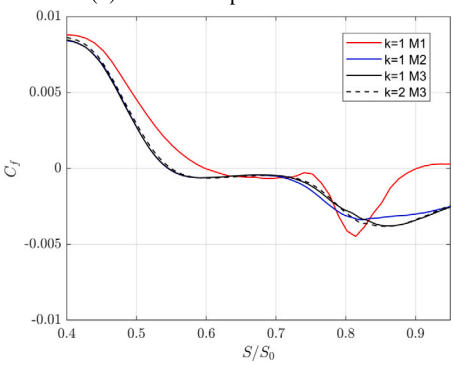

(c) Skin friction coefficient: k=1

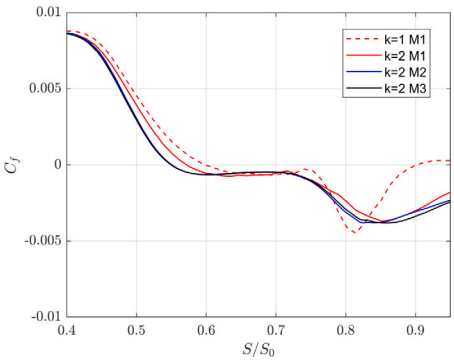

(d) Skin friction coefficient: k=2

Fig. 7. Predictions at $Re_{2,is}$ = 100,000 and Tu = 0.9%.

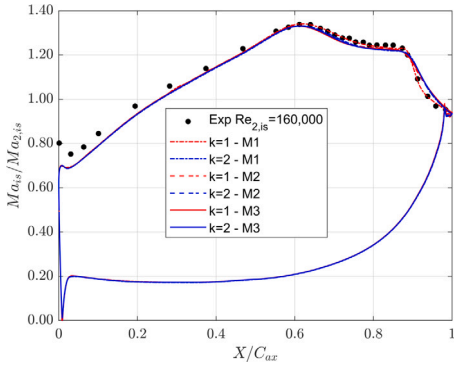

(a) Blade loading

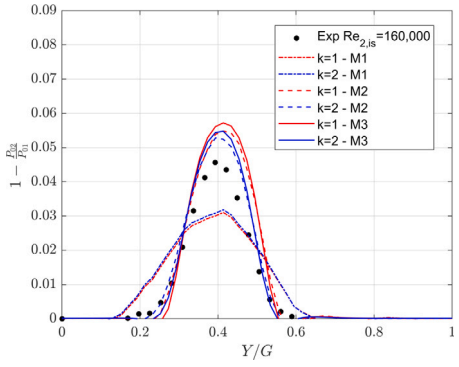

(b) Outlet total pressure losses

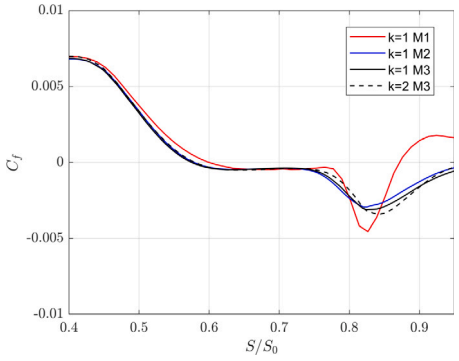

(c) Skin friction coefficient: k=1

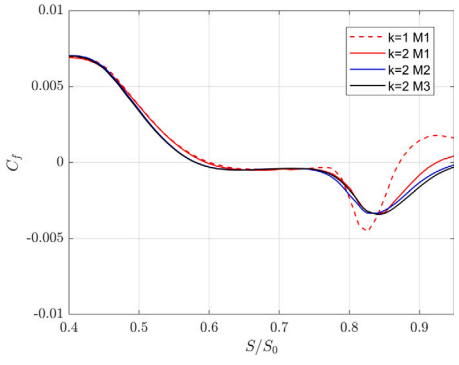

(d) Skin friction coefficient: k=2

Fig. 8. Predictions at $Re_{2,is}$ = 160,000 and Tu = 0.9%.

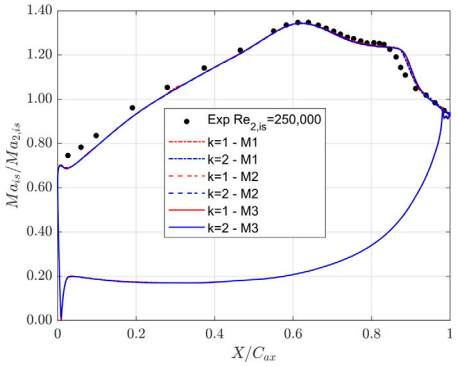

(a) Blade loading

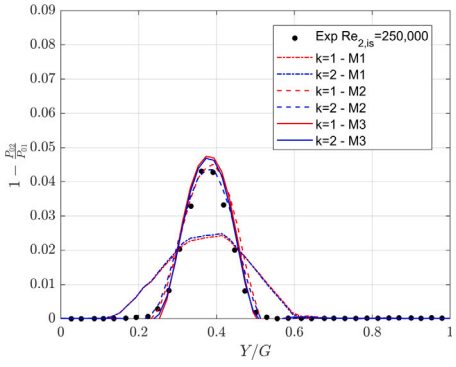

(b) Outlet total pressure losses

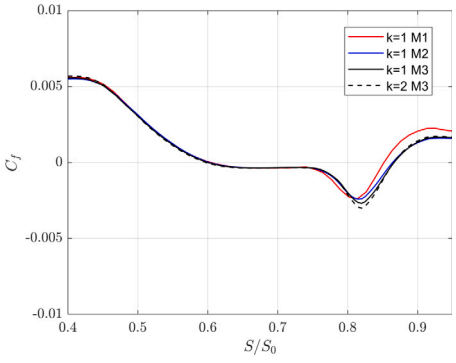

(c) Skin friction coefficient: k=1

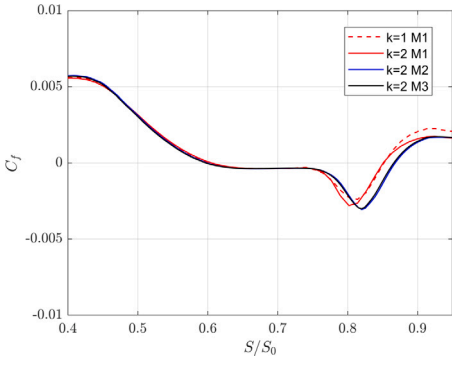

(d) Skin friction coefficient: k=2

Fig. 9. Predictions at $Re_{2,is} = 250{,}000$ and Tu = 0.9%.

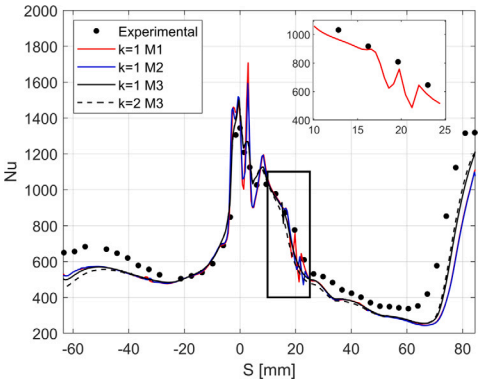

(a) Second order discretization

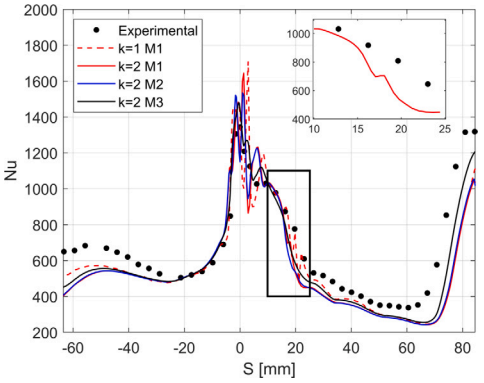

(b) Third order discretization

Fig. 10. MUR218.

the close-up view shows how wiggles in the Nusselt number in the 15 mm < S < 20 mm are removed when a higher discretization order is used the coarsest mesh. The same cannot be said for the LE region, where spikes of the Nusselt number are found for coarse meshes, which can be efficiently removed only by means of an improved spatial discretization of the geometry in the highly curved region.

As a last remark in the heat transfer prediction section, it can be said that the impact of the higher reconstruction order on the prediction of the heat transfer over the high-pressure vane is somehow limited compared to the aerodynamic test cases shown in Sec. 4.1 and 4.2. This is probably adduced to the high Reynolds number of the configuration, which exacerbates the effect of Reynolds dependence, discussed for the T106C cascade.

4.4. Three-dimensional low-pressure turbine cascade

The last test case is the three-dimensional flow field arising in the T106A low-pressure turbine cascade. The T106A represents a high-lift low-pressure turbine blade, investigated by [14]. The operating conditions used in the present investigation are $Ma_{2,is} = 0.59$ and $Re_{2,is} = 120{,}000$. The boundary conditions are set imposing a total pressure profile, with a constant incidence angle. On the other hand, the inlet turbulence is specified using a turbulent length scale equal to 4% of blade's chord and the turbulence intensity retrieved from the paper of [32]. The analysis is performed using two-dimensional meshes which are extruded in the spanwise direction. Two different meshes, with respectively 2.2 M and 7.6 M elements, have been used. In both cases, both the profile boundary layer and the endwall boundary layer are resolved enforcing a $y^+ < 1$. The LE and TE details of both meshes are reported in Fig. 13.

The analysis of the cascade is dedicated to the predictions of the endwall flow and the associated loss distribution. Fig. 14 shows the loading (in terms of pressure coefficient) at two different spanwise positions: the hub endwall and at mid-span. The latter is defined as:

$$C_p = \frac{P - P_2}{P_{01} - P_2} \tag{24}$$

The mid-span pressure coefficient distribution is well predicted by the simulations, even if the peak velocity is slightly overestimated. Over the endwall, the loading is over-predicted due to the lower pressure coefficient on the suction side. As far as the outlet flow field is concerned, the predictions of the mass flow averaged outlet flow angle and total pressure losses are summarized in Fig. 15. The total pressure loss coefficient ω is defined as:

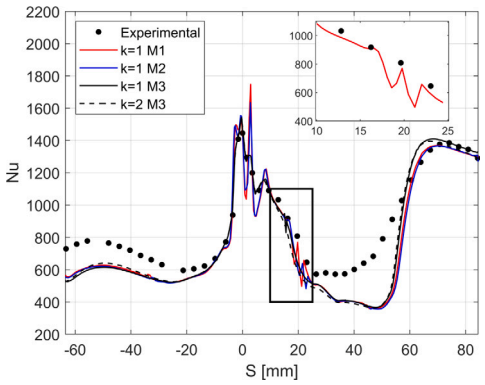

(a) Second order discretization

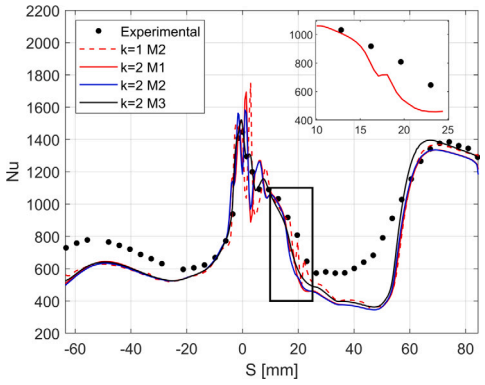

(b) Third order discretization

Fig. 11. MUR237.

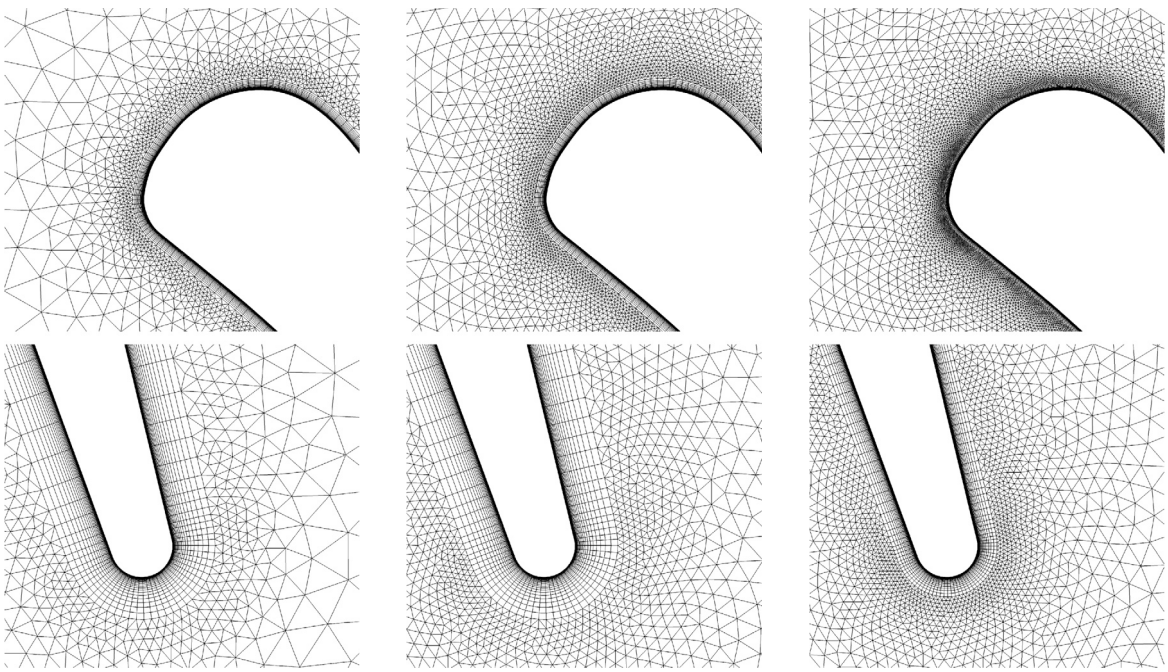

(a) M1 (b) M2 (c) M3

Fig. 12. LS89 - LE and TE mesh details.

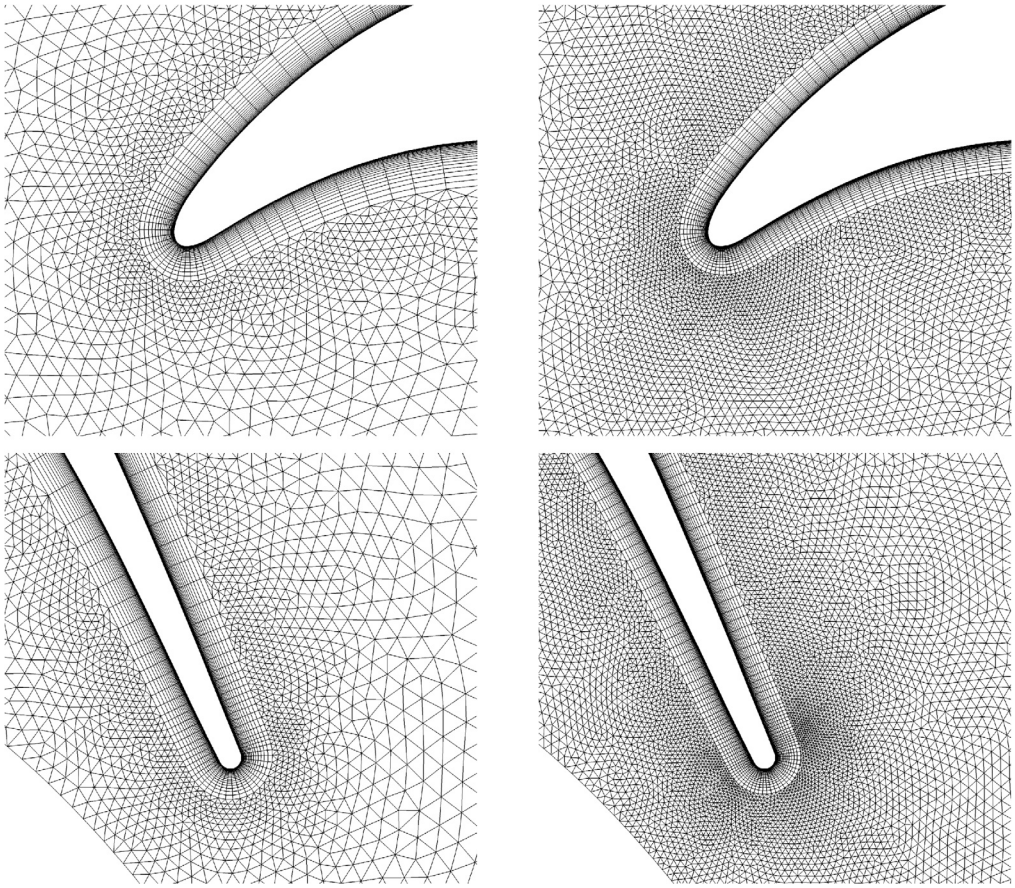

Fig. 13. T106A - LE and TE mesh details.

$$\omega = \frac{P_{01} - P_{02}}{P_{01} - P_2} \tag{25}$$

The simulations underestimate the losses in the endwall region and the spanwise position of the loss peak. On the other hand, the peak loss is overestimated. It must be said that these results are in line with the predictions shown by [32] and [15]. As far as the angle is concerned, the CFD manages to reproduce correctly the over-turning close to the endwall, while the underturning predicted in the loss core is underestimated by approximately 2°. Similarly to the results shown for the T106C, the impact of the high-order discretization is limited to some local flow features in the wake and cascades loss region. The local streamwise vorticity coefficient is shown in Fig. 16, where the streamwise vorticity coefficient is shown for the plane X = 0.9 c_{ax}. The coefficient is defined according to Eq. (26) where β represents the flow angle at mid-span, while Ω_X and Ω_Y represent the axial and pitchwise vorticity, respectively.

$$C_{\omega s} = c\frac{\Omega_X \times cos(\beta_{ms}) + \Omega_Y \times sin(\beta_{ms})}{V_{2,is}} \tag{26}$$

The vortical structures highlighted are referred to the Passage Vortex (PV), the Pressure Side leg of the horseshoe vortex (HVPS), the Corner Vortex (CV) and the Wall Vortex (WV), which is generated under the pitchwise/spanwise migration of the PV+HVPS system. Their interaction is the main driver for loss generation. In order to understand the differences between the various discretization orders, a close-up view of the total pressure loss coefficient contours is shown in Fig. 17. For this analysis, the results of the k = 2 M2 simulation are taken as reference. Regarding the simulation adopting M1, the averaged outlet losses showed that the increase of the discretization order mainly impacts the endwall region loss, which is more in accordance with the results obtained with mesh M2. On the other hand, greater differences can be seen in correspondence of the cascade flow. As a matter of fact, while both simulations predict the same loss (and consequently flow) pattern, the local shape of the structures changes for a third order discretization and get closer to the results obtained for the finer mesh M1. The major difference is noted in the region of high loss between the WV and the HVPS. While the k = 2, M2 solution is recovered by the k = 2, M1 setup to a better extent, the results obtained for k = 1, M1 are more diffused and the isolines are also shifted towards the endwall. The non-dimensional convergence time for the three-dimensional test case are reported in Table 10.

Table 10
T106A non-dimensional convergence time.

	k = 0	k = 1	k = 2
M1	0.0994	0.1926	0.2403
M2	0.5628	0.8846	1.0000

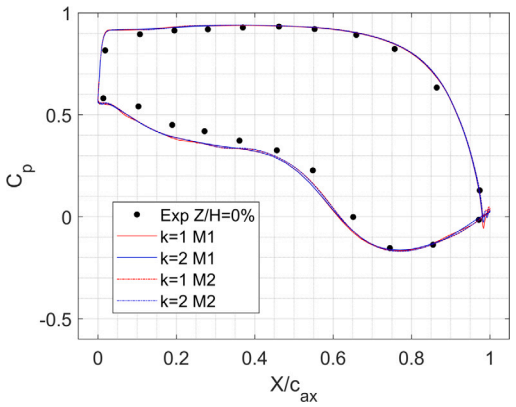

(a) Z/H=0%

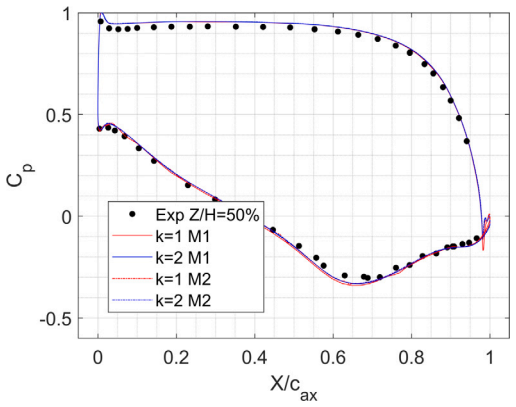

(b) Z/H=50%

Fig. 14. T106A - Loading predictions.

5. Conclusions

In this paper, the implementation of a high-order reconstruction method based on a Least-Square polynomial approximation of flow variables, is implemented into the in-house Finite Volume solver HybFlow. The validation of the solver has been performed on the transitional zero pressure gradient flow over a flat plate with two different test cases. The solver is able to match the experimental skin friction coefficient. It is shown that the use of Least Square gradients for the computation of source terms leads to a delayed transition, while a Green-Gauss procedure based on the high-order reconstruction of flow variables at cell faces is to be preferred. Moreover, it is demonstrated that the high order method on coarser meshes effectively recovers lower order solution over finer spatial discretizations. The solver is later applied to the solution of the T106C low-pressure turbine blade, in a wide range of operating Reynolds numbers. The solver properly predicts the blade loading, while there is an overestimation of the total pressure deficit in the wake center for all investigated conditions. The high order discretization allows to improve the prediction of the laminar separation bubble size on coarse meshes, improving the match with experimental results. The third test case analyzes the heat transfer over the LS89 vane for two different levels of turbulence intensity. For low turbulence intensity the experimental Nusselt number is correctly predicted, with a small underestimation of experimental results over the suction side and in the last part of the pressure side. Bigger differences are present in the high turbulence case. In both cases, the effect of a third order discretization is instead limited compared to a common second order. The last test case reported is the three-dimensional flow field in the T106A linear cascade. The analysis reports the prediction of the endwall flow field, in terms of losses and flow angle. Similarly to the two-dimensional test cases, the higher order discretization increases resolution in the prediction of local flow features, as the loss associated to the secondary flows, while the effect over averaged results is limited. The latter is mainly driven by mesh density. It can be concluded that the use of a higher order reconstruction for turbomachinery test cases is beneficial for a better resolution of local features like separation bubbles and

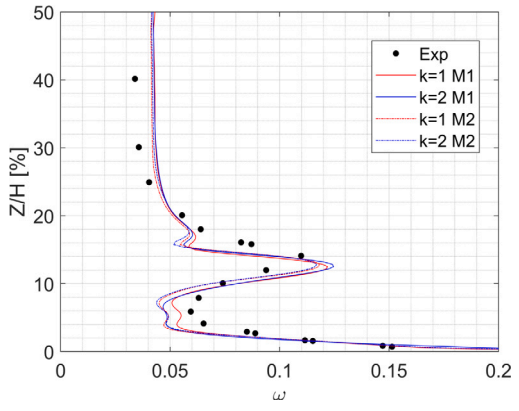

(a) Total pressure loss coefficient

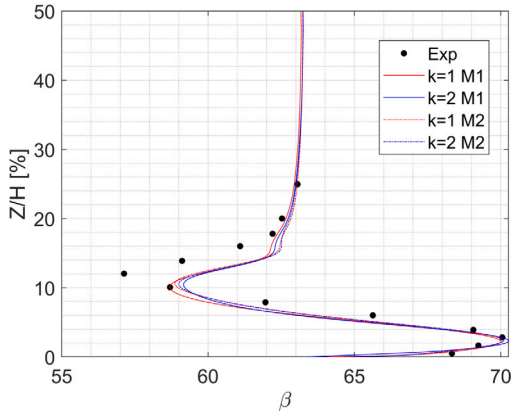

(b) Flow angle

Fig. 15. T106A - Outlet predictions.

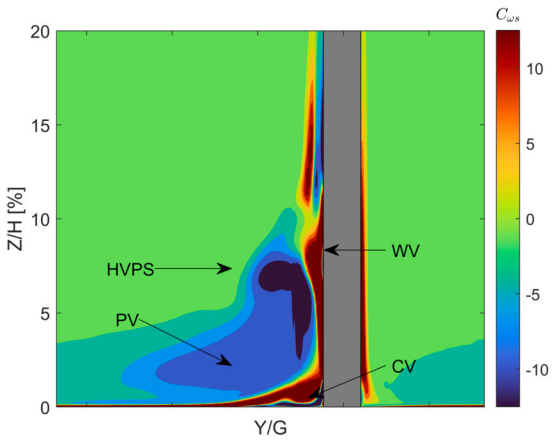

Fig. 16. T106A - Streamwise vorticity coefficient at $X/c_{ax} = 0.9$.

developing vortex due to the lower dissipation associated to reconstruction orders higher than the second. Additional work will be performed on the analysis of the impact of the choice of solution variables. Moreover, considering the better spectral properties of high-order methods, additional effort will be made to analyze the impact of the discretization order in scale-resolving simulations such as the Implicit Large-Eddy Simulation (ILES).

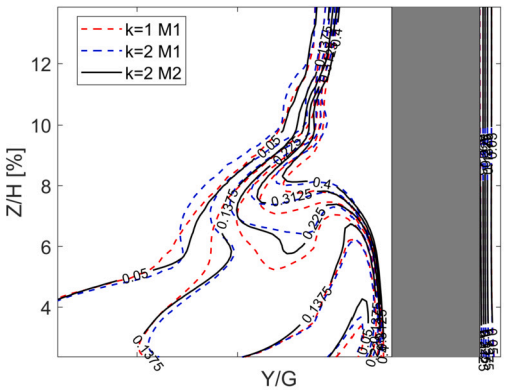

Fig. 17. T106A - Total pressure loss coefficient at $X/c_{ax} = 0.9$.

6. Data availability statement

Data obtained using the in-house solver HybFlow and associated with the present study has not been deposited into a publicly available repository. Also, the authors do not have permission to share the experimental data associated with the present study through a publicly available repository.

7. Nomenclature

c	Blade chord
C_f	Skin friction coefficient
c_{ax}	Blade axial chord
C_p	Pressure coefficient
$C_{\omega s}$	Streamwise vorticity coefficient
G	Blade pitch
k	polynomial order
ILS	Integral length scale
LE	Leading edge
LSB	Laminar separation bubble
LSQ	Least square
Ma	Mach number
Nu	Nusselt number
N_{DOF}	Number of degrees of freedom
$N_{profile}$	Number of points over the profile
N_{sub}	Number of subdomains
P	Pressure
Re	Reynolds number
Re_x	Distance based Reynolds number
S	Curvilinear abscissa
S_0	Curve length
s^+	Dimensionless streamwise spacing
TE	Trailing edge
Tu	Turbulence intensity
U	Velocity
U_∞	Free-stream velocity
X	Axial coordinate
x^+	Dimensionless axial spacing
Y	Pitchwise coordinate
y^+	Dimensionless wall distance
VR	Viscosity ratio
Z	Spanwise coordinate
R	Non-linear residuals
w	Conservative variables vector
β	Flow angle
k	Turbulent kinetic energy and polynomial order

μ_t	Turbulent viscosity
$\overline{v^2}$	Three-dimensional velocity fluctuations energy
ω	Specific dissipation rate (total pressure loss coefficient)
$_2$	Referred to the outlet measurement plane
$_1$	Referred to the inlet measurement plane
$_0$	Total condition
$_{is}$	Referred to isentropic conditions

CRediT authorship contribution statement

Nicola Rosafio: Writing – review & editing, Writing – original draft, Visualization, Validation, Software, Methodology, Investigation, Formal analysis, Data curation, Conceptualization. **Simone Salvadori:** Writing – review & editing, Writing – original draft, Visualization, Supervision, Software, Resources, Methodology, Conceptualization. **Daniela Anna Misul:** Writing – review & editing, Writing – original draft, Supervision, Resources, Project administration, Funding acquisition, Conceptualization.

Declaration of competing interest

The authors declare that they have no known competing financial interests or personal relationships that could have appeared to influence the work reported in this paper.

References

[1] H.D. Akolekar, Y. Zhao, R.D. Sandberg, R. Pacciani, Integration of machine learning and computational fluid dynamics to develop turbulence models for improved low-pressure turbine wake mixing prediction, Journal of Turbomachinery 143 (2021) 121001, https://doi.org/10.1115/1.4051417.

[2] W. Anderson, D.L. Bonhaus, An implicit upwind algorithm for computing turbulent flows on unstructured grids, Comput. Fluids 23 (1994) 1–21, https://doi.org/10.1016/0045-7930(94)90023-X.

[3] T. Arts, M. Lambert de Rouvroit, A.W. Rutherford, Aero-thermal investigation of a highly-loaded transonic linear turbine guide vane cascade, NASA STI/Recon Technical Report N 91, von Karman Institute for Fluid Dynamics, 1990.

[4] J. Babajee, T. Arts, Investigation of the laminar separation-induced transition with the $\gamma - \tilde{R}e_{\theta,t}$ transition model on low-pressure turbine rotor blades at steady conditions, in: Volume 8: Turbomachinery, Parts A, B, and C, 2012, pp. 1167–1178.

[5] T. Barth, P. Frederickson, Higher order solution of the Euler equations on unstructured grids using quadratic reconstruction, https://doi.org/10.2514/6.1990-13, 1990.

[6] F. Bassi, L. Botti, A. Colombo, A. Crivellini, N. Franchina, A. Ghidoni, Assessment of a high-order accurate discontinuous Galerkin method for turbomachinery flows, Int. J. Comput. Fluid Dyn. 30 (2016) 307–328, https://doi.org/10.1080/10618562.2016.1198783.

[7] F. Bassi, S. Rebay, A high order discontinuous Galerkin method for compressible turbulent flows, in: Discontinuous Galerkin Methods, Springer Berlin Heidelberg, Berlin, Heidelberg, 2000, pp. 77–88.

[8] A. Benyahia, Mise en oeuvre et évaluation d'un modèle de transition à équations de transport pour la simulation d'écoulements en turbomachines, https://api.semanticscholar.org/CorpusID:127498584, 2012.

[9] V. Brunet, E. Croner, A. Minot, J. de Laborderie, E. Lippinois, S. Richard, J.F. Boussuge, J. Dombard, F. Duchaine, L. Gicquel, T. Poinsot, G. Puigt, G. Staffelbach, L. Segui, O. Vermorel, N. Villedieu, J.S. Cagnone, K. Hillewaert, M. Rasquin, G. Lartigue, V. Moureau, V. Couaillier, E. Martin, M. de la Llave Plata, J.M. Le Gouez, F. Renac, Comparison of various CFD codes for LES simulations of turbomachinery: from inviscid vortex convection to multi-stage compressor, Volume 2C: Turbomachinery, V02CT42A013, https://doi.org/10.1115/GT2018-75523, 2018.

[10] A. Cassinelli, F. Montomoli, P. Adami, S.J. Sherwin, High fidelity spectral/hp element methods for turbomachinery, Volume 2C: Turbomachinery, V02CT42A020, https://doi.org/10.1115/GT2018-75733, 2018.

[11] CentaurSoft, Centaur, https://www.centaursoft.com, 2021.

[12] J. Coupland, Ercoftac special interest group on laminar to turbulent transition and retransition: T3a and t3b test cases, A309514, 1990.

[13] M. Dellacasagrande, D. Lengani, E. Bertolini, W. Sanz, Correlated pressure–velocity instability in a transonic high-pressure turbine blade, J. Turbomach. 145 (2022) 041015, https://doi.org/10.1115/1.4055971.

[14] A. Duden, L. Fottner, Influence of taper, Reynolds number and Mach number on the secondary flow field of a highly loaded turbine cascade, Proc. Inst. Mech. Eng. A, J. Power Energy 211 (1997) 309–320, https://doi.org/10.1177/095765099721100401.

[15] M. Errante, A. Ferrero, F. Larocca, Simulation of secondary flows in turbomachinery by the discontinuous Galerkin method, AIP Conf. Proc. 2611 (2022) 050005, https://doi.org/10.1063/5.0120392.

[16] F. Haider, Discrétisation en maillage non structuré général et applications LES, Ph.D. thesis, Université Pierre et Marie Curie-Paris VI, 2009.

[17] K. Hillewaert, C.C. de Wiart, G. Verheylewegen, T. Arts, Assessment of a high-order discontinuous Galerkin method for the direct numerical simulation of transition at low-Reynolds number in the T106C high-lift low pressure turbine cascade, Volume 2B: Turbomachinery, V02BT39A034, https://doi.org/10.1115/GT2014-26739, 2014.

[18] S. Hoshyari, E. Mirzaee, C. Ollivier-Gooch, Efficient convergence for a higher-order unstructured finite volume solver for compressible flows, AIAA J. 58 (2020) 1490–1505, https://doi.org/10.2514/1.J058537.

[19] S. Hu, C. Zhou, Z. Xia, S. Chen, LES and CDNS investigation of T106C low pressure turbine, Volume 2C: Turbomachinery, V02CT39A029, https://doi.org/10.1115/GT2016-56838, 2016.

[20] L. Ivan, C.P. Groth, High-order solution-adaptive central essentially non-oscillatory (ceno) method for viscous flows, J. Comput. Phys. 257 (2014) 830–862, https://doi.org/10.1016/j.jcp.2013.09.045.

[21] A. Jalali, C. Ollivier-Gooch, Higher-order unstructured finite volume rans solution of turbulent compressible flows, Comput. Fluids 143 (2017) 32–47, https://doi.org/10.1016/j.compfluid.2016.11.004.

[22] S. Jee, J. Joo, G. Medic, Large-eddy simulation of a high-pressure turbine vane with inlet turbulence, in: Turbo Expo: Power for Land, Sea, and Air, Volume 2D: Turbomachinery, 2016.

[23] M. Lopez, D. Walters, Prediction of transitional and fully turbulent flow using an alternative to the laminar kinetic energy approach, J. Turbul. 17 (2015) 1–21, https://doi.org/10.1080/14685248.2015.1062509.

[24] D. Mavriplis, Revisiting the least-squares procedure for gradient reconstruction on unstructured meshes, https://doi.org/10.2514/6.2003-3986, 2003.

[25] A. Menasria, P. Brenner, P. Cinnella, Improving the treatment of near-wall regions for multiple-correction k-exact schemes, Comput. Fluids 181 (2019) 116–134, https://doi.org/10.1016/j.compfluid.2019.01.009.
[26] C. Michalak, C. Ollivier-Gooch, Globalized matrix-explicit Newton-gmres for the high-order accurate solution of the Euler equations, Comput. Fluids 39 (2010) 1156–1167, https://doi.org/10.1016/j.compfluid.2010.02.008.
[27] J. Michálek, M. Monaldi, T. Arts, Aerodynamic performance of a very high lift low pressure turbine airfoil (T106C) at low Reynolds and high Mach number with effect of free stream turbulence intensity, J. Turbomach. 134 (2012) 061009, https://doi.org/10.1115/1.4006291.
[28] C. Ollivier-Gooch, High-order ENO schemes for unstructured meshes based on least-squares reconstruction, https://doi.org/10.2514/6.1997-540, 1997.
[29] C. Ollivier-Gooch, A. Jalali, Accuracy assessment of finite volume discretizations of diffusive fluxes on unstructured meshes, in: 50th AIAA Aerospace Sciences Meeting Including the New Horizons Forum and Aerospace Exposition, 2012.
[30] C. Ollivier-Gooch, M. Van Altena, A high-order-accurate unstructured mesh finite-volume scheme for the advection–diffusion equation, J. Comput. Phys. 181 (2002) 729–752, https://doi.org/10.1006/jcph.2002.7159.
[31] R. Pacciani, M. Marconcini, A. Fadai-Ghotbi, S. Lardeau, M.A. Leschziner, Calculations of high-lift cascades in low pressure turbine conditions using a three-equation model, in: Volume 7: Turbomachinery, Parts A and B, 2009, pp. 433–442.
[32] R. Pichler, Y. Zhao, R. Sandberg, V. Michelassi, R. Pacciani, M. Marconcini, A. Arnone, Large-eddy simulation and RANS analysis of the end-wall flow in a linear low-pressure turbine cascade, Part I: flow and secondary vorticity fields under varying inlet condition, J. Turbomach. 141 (2019) 121005, https://doi.org/10.1115/1.4045080.
[33] G. Pont, P. Brenner, P. Cinnella, B. Maugars, J.C. Robinet, Multiple-correction hybrid k-exact schemes for high-order compressible rans-les simulations on fully unstructured grids, J. Comput. Phys. 350 (2017) 45–83, https://doi.org/10.1016/j.jcp.2017.08.036.
[34] P. Roe, Approximate Riemann solvers, parameter vectors, and difference schemes, J. Comput. Phys. 43 (1981) 357–372, https://doi.org/10.1016/0021-9991(81)90128-5.
[35] Y. Saad, M.H. Schultz, Gmres: a generalized minimal residual algorithm for solving nonsymmetric linear systems, SIAM J. Sci. Stat. Comput. 7 (1986) 856–869, https://doi.org/10.1137/0907058.
[36] D.K. Walters, D. Cokljat, A three-equation eddy-viscosity model for Reynolds-averaged Navier–Stokes simulations of transitional flow, J. Fluids Eng. 130 (2008) 121401, https://doi.org/10.1115/1.2979230.
[37] X. Wang, B. Cui, Z. Xiao, Numerical investigation on ultra-high-lift low-pressure turbine cascade aerodynamics at low Reynolds numbers using transition-based turbulence models, J. Turbul. 22 (2021) 114–139, https://doi.org/10.1080/14685248.2020.1849712.
[38] D.C. Wilcox, Turbulence Modeling for CFD, vol. 2, DCW Industries Inc., La Canada, CA, 1998.
[39] S. Xu, P. Mohanamuraly, D. Wang, J.D. Müller, Newton–Krylov solver for robust turbomachinery aerodynamic analysis, AIAA J. 58 (2020) 1320–1336, https://doi.org/10.2514/1.J058523.
[40] M. Yao, L. He, Implicit discontinuous Galerkin solution on unstructured mesh for turbine blade secondary flow, J. Turbomach. 142 (2019) 011004, https://doi.org/10.1115/1.4045551.